


Article

A Station-Keeping Control Strategy for a Symmetrical Spacecraft Utilizing Hybrid Low-Thrust Propulsion in the Heliocentric Displaced Orbit

Tengfei Zhang ¹, Rongjun Mu ^{1,*}, Yilin Zhou ¹, Zizheng Liao ¹, Zhewei Zhang ², Bo Liao ³ and Chuang Yao ³¹ School of Astronautics, Harbin Institute of Technology, Harbin 150001, China² Aerospace System Engineering Shanghai, Shanghai 201109, China; zhangzw_ases@163.com³ Shanghai Institute of Satellite Engineering, Shanghai 201109, China; angel885201@126.com (B.L.); yaochuang0@126.com (C.Y.)

* Correspondence: murjun@163.com

Abstract: The solar sail spacecraft utilizing a hybrid approach of solar sail and solar electric propulsion in the heliocentric displaced orbit is affected by external disturbances, internal unmodeled dynamics, initial injection errors, and input saturation. To solve the station-keeping control problem under such complex conditions, an adaptive control strategy is proposed. First, the dynamical equations of the spacecraft utilizing hybrid low-thrust propulsion in the cylindrical coordinate system are derived. Second, the combined disturbance acceleration introduced by external disturbances and internal unmodeled dynamics is constructed, and a radial basis function neural network estimator is designed to estimate it online in real time. Third, an adaptive high-performance station-keeping controller based on an improved integral sliding surface and multivariate super-twisting sliding mode approaching law is designed. Then, stability analysis is conducted using Lyapunov theory, adaptive laws are designed, and the introduced virtual control accelerations are converted into actual control variables. Finally, simulations are conducted under different simulation conditions based on the disturbance sources. The results show that although the use of hybrid low-thrust propulsion breaks the symmetry of the solar sail in configuration, the proposed control strategy can effectively achieve the station-keeping and disturbance estimation of the spacecraft with only a small amount of propellant consumed and position tracking errors up to decimeters.

Keywords: solar sail spacecraft; station-keeping; radial basis function neural network; improved integral sliding surface; multivariate super-twisting sliding mode approaching law



Citation: Zhang, T.; Mu, R.; Zhou, Y.; Liao, Z.; Zhang, Z.; Liao, B.; Yao, C. A Station-Keeping Control Strategy for a Symmetrical Spacecraft Utilizing Hybrid Low-Thrust Propulsion in the Heliocentric Displaced Orbit. *Symmetry* **2023**, *15*, 1549. <https://doi.org/10.3390/sym15081549>

Academic Editors:

Florentin Smarandache and
Quanxin Zhu

Received: 14 June 2023

Revised: 23 July 2023

Accepted: 4 August 2023

Published: 6 August 2023



Copyright: © 2023 by the authors. Licensee MDPI, Basel, Switzerland. This article is an open access article distributed under the terms and conditions of the Creative Commons Attribution (CC BY) license (<https://creativecommons.org/licenses/by/4.0/>).

1. Introduction

In addition to being subjected to the gravitational force of celestial bodies, a solar sail is also subjected to solar radiation pressure, which cannot vary arbitrarily in space. The solar sail spacecraft is a spacecraft that generates thrust using solar photons interacting with a high area ratio sail surface to achieve interplanetary travel [1]. The solar sail spacecraft is actually a complex dynamical system in which orbital motion, attitude motion, and structural vibrations are coupled with each other. The standard for evaluating a solar sail dynamics model is that it should accurately reflect dynamical characteristics such as high flexibility, low stiffness, weak damping, and low fundamental frequency and modal density [2]. The first successful application of the solar sail in the world was the IKAROS (Interplanetary Kite-craft Accelerated by Radiation of the Sun, IKAROS), which was launched in 2010 [3].

At present, research on station-keeping control for solar sails is dominated by linear control methods. The basic principle of linear control is to first linearize the orbital dynamics equations, then use the reference orbit as the control command, and use various linear feedback control methods to design the station-keeping control law, such as linear state

feedback control [4–6], PID control [7], and LQR control [8–11]. To update the control law for subsequent orbits, Moore and Ceriotti proposed a new method on the basis of the use of a Control Transition Matrix and linearization [12]. Additionally, another major research approach for the station-keeping control of solar sails is auto disturbance rejection control (ADRC) [13–19].

The solar sail spacecraft that utilizes hybrid small-thrust propulsion [20,21] is a new continuous small-thrust spacecraft combining the solar sail propulsion system and the solar electric propulsion system, which is suitable for complex orbital missions. On the one hand, it has the dual advantages of no energy consumption for solar sail propulsion and high efficiency for solar electric propulsion. On the other hand, it is one that overcomes the shortcomings of solar sails that cannot provide a propulsive part pointing in the direction of the sun. Simo and McInnes [22] proposed a hybrid sail feedback linearized orbital controller, where they compensated for the nonlinear terms in the model with closed-loop feedback and designed a state error PD control law for the compensated linear system. Heiligers et al. [23] designed a geosynchronous displaced orbit control method based on a hybrid propulsion solar sail, compared the fuel consumption of the hybrid propulsion solar sail and pulse control, and found that fuel consumption can be effectively reduced using a hybrid propulsion solar sail.

The newly launched Starlink satellite “V2 mini” utilizes argon Hall thrusters. The advent of this technology has made it possible to achieve hybrid orbit control without significantly increasing the mass of the solar sail spacecraft. The greatest advantage of argon electric thrusters over xenon or krypton Hall thrusters currently in use is their extremely low cost. As an example, 1 kg of high-purity xenon gas sells for tens of thousands of CNY, while the same quality of high-purity argon gas costs only a few CNY [24].

The heliocentric displaced orbit is a non-Kepler periodic orbit displaced above the sun and formed by the mutual balance of spacecraft propulsion and gravity. Due to its special space position, it provides an ideal platform for deep space relay communication, sun–Earth observation, and other orbital missions [25]. McInnes [26] and Bookless [27] summarized and analyzed the dynamic characteristics of different types of displaced orbits, and the results showed that the orbits under certain parameters are unstable, requiring station-keeping techniques to ensure the stable operation of a spacecraft in the target displaced orbit. Qian et al. [28] adopted an LQR to design an orbit-keeping control law based on the linearized equation of state of the solar sail spacecraft near the reference heliocentric displaced orbit. Zhang et al. [29] used the ADRC with low model dependence to design a station-keeping controller for a hybrid small-thrust spacecraft, and achieved good results. However, the parameter tuning is relatively cumbersome, and there is a significant overshoot, which means that the track position deviates significantly at one point. Chen et al. [30] designed a control law based on a modified conditional integral sliding surface and combined it with an adaptive method to estimate uncertain parameters online.

Most of the above research on solar sail spacecraft in the heliocentric displaced orbit has linearized dynamic equations, resulting in high dependence on accurate models. Some studies have ignored the effects of model uncertainty due to modeling errors, complex deep space environments, etc. Meanwhile, single solar sail propulsion suffers from slow convergence speed and low control accuracy. And, complex conditions such as external disturbances, internal unmodeled dynamics, initial injection errors, and input saturation further increase the difficulty of the controller design. An adaptive high-performance sliding mode control strategy is proposed for the station-keeping problem under these complex conditions. Compared to the existing literature, the main contributions of this article include the following:

- (1) A high-performance station-keeping controller, designed on the basis of an improved integral sliding mode and multivariate super-twisting sliding mode approaching law, has fast orbital tracking speed and high control accuracy;
- (2) The weight coefficient matrix of the radial basis function (RBF) neural network is used as an uncertain parameter, and its adaptive law is designed using Lyapunov stability

analysis. On this basis, an RBF neural network estimator is designed, which can estimate online and compensate for the combined disturbance acceleration constructed from external disturbances and internal unmodeled dynamics;

(3) Transforming the virtual control acceleration introduced into actual control variables and obtaining the optimal control variable with the objective of minimizing propellant consumption of the argon Hall thruster can solve the problem of low control accuracy caused by linearized dynamic equations.

(4) Although the use of hybrid low-thrust propulsion breaks the symmetry of the solar sail in the configuration, the proposed control strategy requires only a small amount of propellant consumption to effectively achieve the station-keeping control of the spacecraft.

2. Orbit Dynamic Model

2.1. Definition of Coordinate System and Attitude Angle

To derive the orbit dynamics model of a solar sail spacecraft utilizing hybrid small-thrust propulsion in a heliocentric displaced orbit, the following coordinate system is defined:

(1) Heliocentric displaced orbit coordinate system: $o\text{-}xyz$. As shown in Figure 1, the origin is located at the center o of the sun. The oxy plane is parallel to the displaced orbital plane. The ox -axis points to the vernal equinox of the J2000 ephemeris, and the oz -axis points to the direction of the angular velocity of Earth’s revolution. The ox -axis, the oy -axis, and the oz -axis form a right-handed coordinate system.

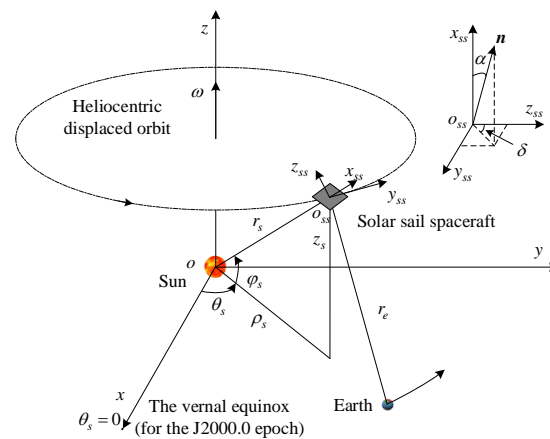


Figure 1. Displaced orbit and orbital coordinate system of the solar sail spacecraft.

(2) Orbital coordinate system: $o_{ss}\text{-}x_{ss}y_{ss}z_{ss}$. The origin is located at the center o_{ss} of the solar sail spacecraft. The $o_{ss}x_{ss}$ -axis points in the direction of the position vector r_s , and the $o_{ss}y_{ss}$ -axis is perpendicular to the $o_{ss}x_{ss}$ -axis in the plane of the displaced orbit and points in the direction of the spacecraft’s motion. The $o_{ss}x_{ss}$ -axis, the $o_{ss}y_{ss}$ -axis, and the $o_{ss}z_{ss}$ -axis form a right-handed coordinate system. We assumed that the three axis unit vectors were $i_s, j_s,$ and $k_s,$ respectively.

(3) Cylindrical coordinate system: (ρ_s, θ_s, z_s) . ρ_s and z_s denote the orbital radius and orbital height of the displaced orbit, respectively. θ_s is the angle between the projection of the position vector r_s of the solar sail spacecraft in the oxy plane and the ox -axis. We assumed that the unit vectors of the cylindrical coordinate system were $\hat{\rho}, \hat{\theta},$ and $\hat{z},$ respectively.

The transformation matrix of the orbital coordinate system to the heliocentric displaced orbit coordinate system is as follows:

$$C = \begin{bmatrix} \cos \varphi_s & -\sin \varphi_s & 0 \\ 0 & 0 & 1 \\ \sin \varphi_s & \cos \varphi_s & 0 \end{bmatrix} \tag{1}$$

where $\cos \varphi_s = \frac{\rho_s}{\|r_s\|}; \sin \varphi_s = \frac{z_s}{\|r_s\|}.$

Considering the special configuration of the solar sail spacecraft, new attitude angles are defined:

(1) Cone angle α_s . Define \mathbf{n} to represent the unit normal vector of the sail surface. Then, the cone angle α_s is the angle between the unit normal vector \mathbf{n} and the position vector \mathbf{r}_s . $\alpha_s \in [-\pi/2 \ \pi/2]$.

(2) Turning angle δ_s . The turning angle δ_s is the angle between the projection of the normal vector \mathbf{n} in the $y_{ss}o_{ss}z_{ss}$ plane and the $o_{ss}z_{ss}$ axis. $\delta_s \in [-\pi \ \pi]$.

2.2. Displaced Orbital Dynamics

In the system composed of the sun, Earth, and solar sail spacecraft, the heliocentric displaced orbit studied in this paper is relatively close to Earth and Earth's gravity cannot be neglected. The displaced orbits studied in this paper are within the sphere of influence of a celestial body centered on the sun.

Considering the existence of model uncertainty and external disturbances in the displaced orbital motion system, the orbital dynamics equation is as follows:

$$\ddot{\mathbf{r}}_s = -\frac{\mu_s}{\|\mathbf{r}_s\|^3}\mathbf{r}_s + \mathbf{a}_s + \mathbf{a}_{ep} + \mathbf{a}_{\Delta f} + \mathbf{a}_d \quad (2)$$

where μ_s represents the heliocentric gravitational constant; \mathbf{a}_s is the propulsion acceleration under the action of solar radiation pressure; \mathbf{a}_{ep} is the electric propulsion acceleration, $\mathbf{a}_{ep} = [a_{ep,x} \ a_{ep,y} \ a_{ep,z}]$; $\mathbf{a}_{\Delta f}$ is the acceleration introduced by the model uncertainty, mainly including the modeling error of solar radiation pressure propulsion caused by the special flexible configuration of the solar sail (sail membrane fold deformation, structural vibration, etc.); and \mathbf{a}_d is the acceleration introduced by external disturbances, influenced by dynamic uncertainties such as solar storms and micrometeoroids in the environment.

Normalized units are used to simplify the analysis process. The Earth–sun distance is defined by unit length (1 AU), the solar mass is defined by unit mass ($M_s = 1$), and the angular velocity of Earth's revolution is defined by unit angular velocity ($\omega_e = 1$). Then $\mu_s = 1$.

The solar radiation pressure propulsion acceleration is as follows:

$$\mathbf{a}_s = \beta_s \frac{1}{\|\mathbf{r}_s\|^2} \mathbf{n} \cos^2 \alpha_s \quad (3)$$

The unit normal vector \mathbf{n} of the sail surface can be expressed as follows:

$$\mathbf{n} = [\cos \alpha_s \quad \sin \alpha_s \sin \delta_s \quad \sin \alpha_s \cos \delta_s] \begin{bmatrix} \hat{\mathbf{i}}_s \\ \hat{\mathbf{j}}_s \\ \hat{\mathbf{k}}_s \end{bmatrix} \quad (4)$$

It can also be expressed as a cylindrical coordinate, as follows:

$$\mathbf{n} = (\cos \alpha_s \cos \varphi_s - \sin \alpha_s \cos \delta_s \sin \varphi_s) \hat{\boldsymbol{\rho}} + \sin \alpha_s \sin \delta_s \hat{\boldsymbol{\theta}} + (\cos \alpha_s \sin \varphi_s - \sin \alpha_s \cos \delta_s \cos \varphi_s) \hat{\mathbf{z}} \quad (5)$$

There exists a geometrical relationship in the o - xyz coordinate system:

$$\mathbf{r}_s = \boldsymbol{\rho}_s + \mathbf{z}_s \quad (6)$$

Taking the second order derivatives of $\boldsymbol{\rho}_s$ and \mathbf{z}_s , respectively, gives the following:

$$\frac{d^2 \boldsymbol{\rho}_s}{dt^2} = \left[\frac{d^2 \rho_s}{dt^2} - \rho_s \left(\frac{d\theta_s}{dt} \right)^2 \right] \hat{\boldsymbol{\rho}} + \left[2 \left(\frac{d\rho_s}{dt} \right) \left(\frac{d\theta_s}{dt} \right) + \rho_s \frac{d^2 \theta_s}{dt^2} \right] \hat{\boldsymbol{\theta}} \quad (7)$$

$$\frac{d^2 z_s}{dt^2} = \frac{d^2 z_s}{dt^2} \hat{z} \tag{8}$$

Substituting Equations (5) and (6) into Equation (2), the orbital dynamics equations in the form of cylindrical coordinates are obtained as follows:

$$\begin{cases} \ddot{\rho}_s = \rho_s \dot{\theta}_s^2 - \frac{\rho_s}{\|r_s\|^3} + \beta_s \left(\frac{\cos^3 \alpha_s}{\|r_s\|^3} \rho_s - \frac{\sin \alpha_s \cos^2 \alpha_s \cos \delta_s}{\|r_s\|^3} z_s \right) + \\ \quad a_{ep,x} \cos \theta_s + a_{ep,y} \sin \theta_s + a_{fd,1} \\ \ddot{\theta}_s = -\frac{2}{\rho_s} \dot{\rho}_s \dot{\theta}_s + \beta_s \frac{\sin \alpha_s \cos^2 \alpha_s \sin \delta_s}{\rho_s \|r_s\|^2} - \frac{a_{ep,x} \sin \theta_s}{\rho_s} + \\ \quad \frac{a_{ep,y} \cos \theta_s}{\rho_s} + a_{fd,2} \\ \ddot{z}_s = -\frac{z_s}{\|r_s\|^3} + \beta_s \frac{\cos^3 \alpha_s}{\|r_s\|^3} z_s + \beta_s \frac{\sin \alpha_s \cos^2 \alpha_s \cos \delta_s}{\|r_s\|^3} \rho_s + a_{ep,z} + a_{fd,3} \end{cases} \tag{9}$$

where a_{fd} is the combined disturbance acceleration caused by model uncertainty and external disturbances, $a_{fd} = a_{\Delta f} + a_d = [a_{fd,1} \ a_{fd,2} \ a_{fd,3}]^T$.

Introducing the virtual control acceleration $u = [u_1 \ u_2 \ u_3]^T$, we can obtain the following:

$$\begin{bmatrix} \ddot{\rho}_s \\ \ddot{\theta}_s \\ \ddot{z}_s \end{bmatrix} = \begin{bmatrix} a_{\rho_s} + a_{fd,1} \\ a_{\theta_s} + a_{fd,2} \\ a_{z_s} + a_{fd,3} \end{bmatrix} + \begin{bmatrix} u_1 \\ u_2 \\ u_3 \end{bmatrix} \tag{10}$$

where

$$\begin{cases} a_{\rho_s} = \rho_s \dot{\theta}_s^2 - \frac{\rho_s}{\|r_s\|^3} \\ a_{\theta_s} = -\frac{2}{\rho_s} \dot{\rho}_s \dot{\theta}_s \\ a_{z_s} = -\frac{z_s}{\|r_s\|^3} \end{cases} \tag{11}$$

$$\begin{cases} u_1 = \beta_s \left(\frac{\cos^3 \alpha_s}{\|r_s\|^3} \rho_s - \frac{\sin \alpha_s \cos^2 \alpha_s \cos \delta_s}{\|r_s\|^3} z_s \right) + \\ \quad a_{ep,x} \cos \theta_s + a_{ep,y} \sin \theta_s \\ u_2 = \beta_s \frac{\sin \alpha_s \cos^2 \alpha_s \sin \delta_s}{\rho_s \|r_s\|^2} - \frac{a_{ep,x} \sin \theta_s}{\rho_s} + \frac{a_{ep,y} \cos \theta_s}{\rho_s} \\ u_3 = \beta_s \frac{\cos^3 \alpha_s}{\|r_s\|^3} z_s + \beta_s \frac{\sin \alpha_s \cos^2 \alpha_s \cos \delta_s}{\|r_s\|^3} \rho_s + a_{ep,z} \end{cases} \tag{12}$$

3. High-Performance Station-Keeping Controller Design

For the dynamical model (10) of the heliocentric displaced orbit, a station-keeping controller based on an RBF neural network estimator, an improved integral sliding surface, and a multivariate super-twisting sliding mode approaching law are designed. The structure of the station-keeping control system is shown in Figure 2.

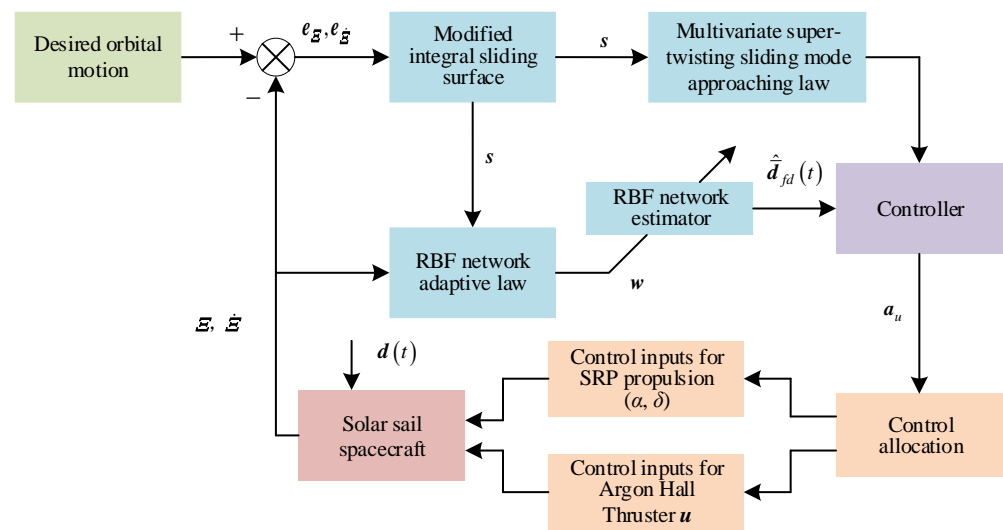


Figure 2. Block diagram of the station-keeping control system for a solar sail spacecraft.

3.1. RBF Neural Network Estimator Design

With excellent local nonlinear approximation, the RBF neural network is a neural network capable of approximating any continuous function with arbitrary accuracy. In practical engineering application systems, it is difficult to accurately measure the combined disturbance acceleration a_{fd} . The station-keeping control of the solar sail spacecraft is realized by designing an RBF neural network estimator to estimate and compensate for the combined disturbance acceleration in real time.

Assuming that the hidden layer has n neurons, a_{fd} is a continuous nonlinear function. Denote $\Xi = [\rho_s \ \theta_s \ z_s]^T$, and take the inputs to the neural network to be $x = [\Xi; \dot{\Xi}]$. $a_{fd,i}(x) (i = 1, 2, 3)$ is approximated by the RBF neural network:

$$a_{fd,i}(x) = w_i^T \chi_i(x) + v_i \tag{13}$$

where $w_i \in \mathfrak{R}^n$ represents the ideal RBF neural network weight; v_i denotes the approximation error, which is a very small real vector; and $\chi_i(x) \in \mathfrak{R}^n$ is the radial basis function of the hidden layer.

The output of the Gaussian radial basis function of the j th ($j = 1, 2, \dots, n$) neuron of the hidden layer is as follows:

$$\chi_{ij}(x) = \exp\left(-\frac{(x - c_{ij})^T(x - c_{ij})}{2\sigma_{ij}^2}\right) \tag{14}$$

where c_{ij} is the center vector of the Gaussian radial basis function, and σ_{ij} represents the width of the Gaussian basis function, which is a positive scalar.

$a_{fd,i}$ is unknown, and the RBF neural network estimator $\hat{a}_{fd,i}(x)$ can be designed to fit it for real-time estimation.

$$\hat{a}_{fd,i}(x) = \hat{w}_i^T \chi_i(x) \tag{15}$$

Those marked with “ $\hat{\cdot}$ ” indicate estimated values. To ensure the convergence of the errors and the real-time estimation, a reasonable adaptive law based on Lyapunov’s stability theory was designed for \hat{w}_i , outlined in Section 3.3.

According to Equations (13) and (15), the estimation error is as follows:

$$e_a = a_{fd,i}(x) - \hat{a}_{fd,i}(x) = \left(w_i^T - \hat{w}_i^T\right) \chi_i(x) + v_i \tag{16}$$

and $\dot{e}_a = -\dot{w}_i^T \chi_i(x)$.

3.2. Control Law Design

For System (10), the cylindrical coordinate error $e = [e_1 \ e_2 \ e_3]^T$ is defined as follows:

$$e = \Xi - \Xi_d \tag{17}$$

where $\Xi_d = [\rho_{s,d} \ \theta_{s,d} \ z_{s,d}]^T$. $\rho_{s,d}$, $\theta_{s,d}$, and $z_{s,d}$ denote nominal orbital radius, nominal orbital angle, and nominal displaced height, respectively.

The designed sliding surface $s_i (i = 1, 2, 3)$ is as follows:

$$\begin{cases} s_i = \dot{e}_i + k_{0i}e_i + k_{1i}w_i \\ \dot{w}_i = [-k_{1i}w_i + \varepsilon_i(1 + \tau_i)\text{sat}(s_i) - \tau_i s_i - \dot{e}_i] / k_{0i} \end{cases} \tag{18}$$

where $k_{0i} > 0; k_{1i} > 0; \tau_i$ is the adjustment factor for the degree of the weakened integral (when $\tau_i = -1$ is a traditional integral sliding surface), $\tau_i > -1$; and ε_i is the thickness of the boundary layer, $\varepsilon_i > 0$. The saturation function is defined as follows:

$$\text{sat}(s_i) = \begin{cases} 1 & s_i > \varepsilon_i \\ s_i / \varepsilon_i & s_i \leq \varepsilon_i \\ -1 & s_i < -\varepsilon_i \end{cases} \tag{19}$$

Then,

$$\dot{w}_i = \begin{cases} e_i - (|s_i| - \varepsilon_i)(1 + \tau_i) / k_{0i} & s_i > \varepsilon_i \\ e_i & s_i \leq \varepsilon_i \\ e_i + (|s_i| - \varepsilon_i)(1 + \tau_i) / k_{0i} & s_i < -\varepsilon_i \end{cases}$$

When s_i is inside the boundary layer, \dot{w}_i acts as a traditional integral. When s_i is outside the boundary layer, the integral term \dot{w}_i is weakened. The extent to which it is weakened can be measured according to $(|s_i| - \varepsilon_i)(1 + \tau_i) / k_{0i}$. It is clear that the extent of weakened demand satisfaction can be obtained through the regulating factor τ_i , $\tau_i \in [-1, k_{0i}|e_i| / (|s_i| - \varepsilon_i) - 1)$. The integral term is weakened so that even under relatively large initial errors and disturbances, the control variable is not prone to jumping, the overshoot can be kept small, and the steady-state error is reduced.

Deriving Equation (18) and substituting Equations (10) and (13) into it, we obtain

$$\begin{bmatrix} \dot{s}_1 \\ \dot{s}_2 \\ \dot{s}_3 \end{bmatrix} = \begin{bmatrix} a_{\rho_s} + w_1^T \chi_1(x) + v_1 - \dot{\rho}_{s,d} + k_{01}e_1 + k_{11}w_1 \\ a_{\theta_s} + w_2^T \chi_2(x) + v_2 - \dot{\theta}_{s,d} + k_{02}e_2 + k_{12}w_2 \\ a_{z_s} + w_3^T \chi_3(x) + v_3 - \dot{z}_{s,d} + k_{03}e_3 + k_{13}w_3 \end{bmatrix} + \begin{bmatrix} u_1 \\ u_2 \\ u_3 \end{bmatrix} \tag{20}$$

The designed multivariate super-twisting sliding mode approaching law is as follows:

$$\begin{cases} \dot{s}_i = -k_{2i}|s_i|^{1/2}\text{sign}(s_i) - k_{3i}s_i + \mu_i \\ \dot{\mu}_i = -k_{4i}\text{sign}(s_i) - k_{5i}s_i \end{cases} \tag{21}$$

where $k_{2i} > 0; k_{3i} > 0; k_{4i} > 0$; and $k_{5i} > 0$.

Substituting Equation (21) into Equation (20), we can obtain the following:

$$\begin{bmatrix} u_1 \\ u_2 \\ u_3 \end{bmatrix} = - \begin{bmatrix} a_{\rho_s} + \mathbf{w}_1^T \boldsymbol{\chi}_1(\mathbf{x}) + v_1 - \dot{\rho}_{s,d} + k_{01}e_1 + k_{11}w_1 \\ a_{\theta_s} + \mathbf{w}_2^T \boldsymbol{\chi}_2(\mathbf{x}) + v_2 - \dot{\theta}_{s,d} + k_{02}e_2 + k_{12}w_2 \\ a_{z_s} + \mathbf{w}_3^T \boldsymbol{\chi}_3(\mathbf{x}) + v_3 - \dot{z}_{s,d} + k_{03}e_3 + k_{13}w_3 \end{bmatrix} + \begin{bmatrix} -k_{21}|s_1|^{1/2}\text{sign}(s_1) - k_{31}s_1 + \mu_1 \\ -k_{22}|s_2|^{1/2}\text{sign}(s_2) - k_{32}s_2 + \mu_2 \\ -k_{23}|s_3|^{1/2}\text{sign}(s_3) - k_{33}s_3 + \mu_3 \end{bmatrix} \quad (22)$$

The designed adaptive sliding mode control law for station-keeping control is as follows:

$$\begin{bmatrix} u_1 \\ u_2 \\ u_3 \end{bmatrix} = - \begin{bmatrix} a_{\rho_s} + \hat{\mathbf{w}}_1^T \boldsymbol{\chi}_1(\mathbf{x}) - \dot{\rho}_{s,d} + k_{01}e_1 + k_{11}w_1 \\ a_{\theta_s} + \hat{\mathbf{w}}_2^T \boldsymbol{\chi}_2(\mathbf{x}) - \dot{\theta}_{s,d} + k_{02}e_2 + k_{12}w_2 \\ a_{z_s} + \hat{\mathbf{w}}_3^T \boldsymbol{\chi}_3(\mathbf{x}) - \dot{z}_{s,d} + k_{03}e_3 + k_{13}w_3 \end{bmatrix} + \begin{bmatrix} -k_{21}|s_1|^{1/2}\text{sign}(s_1) - k_{31}s_1 + \mu_1 \\ -k_{22}|s_2|^{1/2}\text{sign}(s_2) - k_{32}s_2 + \mu_2 \\ -k_{23}|s_3|^{1/2}\text{sign}(s_3) - k_{33}s_3 + \mu_3 \end{bmatrix} \quad (23)$$

3.3. Stability Analysis

In the process of designing the controller, the adaptive law is obtained based on the Lyapunov function, which ensures the stability of the corresponding system. And, the stability of the control system, shown in Figure 2, has not been proven via theoretical derivation. Therefore, in this section, the stability of the above closed-loop system will be analyzed based on the Lyapunov function.

Lemma 1 [31]. For a nonlinear system $\dot{\mathbf{x}} = \mathbf{f}(\mathbf{x}(t))$, assuming the existence of a positive definite function $V_s(\mathbf{x}) \in \mathbb{R}$, this satisfies the following:

$$\dot{V}_s(\mathbf{x}) \leq -\kappa_1 V_s(\mathbf{x}) - \kappa_2 V_s^\gamma(\mathbf{x})$$

where $\kappa_1 > 0$; $\kappa_2 > 0$; $\gamma \in (0, 1)$; $V_0 = V_s(\mathbf{x}(0))$; and the nonlinear system $\dot{\mathbf{x}} = \mathbf{f}(\mathbf{x}(t))$ is finite-time stable.

The convergence time can be given by

$$t_s \leq \frac{1}{\kappa_1(1-\gamma)} \ln \frac{\kappa_1 V_0^{1-\gamma} + \kappa_2}{\kappa_2} \quad (24)$$

Theorem 1. For the orbit dynamics system (10) of a solar sail spacecraft utilizing hybrid small-thrust propulsion in a heliocentric displaced orbit, if its control law is designed as in Equation (23), and if the values of the parameters such as k_{0i} , k_{1i} , k_{2i} , k_{3i} , k_{4i} , and k_{5i} are appropriate, the control system can converge to the sliding surface in finite-time, and the orbital tracking error e of the system can converge asymptotically to zero.

Proof of Theorem 1. The proof process will be divided into two steps. Step 1 proves that the system state converges to the sliding surface in finite-time, and Step 2 proves that after reaching the sliding surface, the orbital tracking error e of the system converges asymptotically to zero.

Substituting Equation (23) into Equation (20), we can obtain the following:

$$\begin{cases} \dot{s}_i = -k_{2i}|s_i|^{1/2}\text{sign}(s_i) - k_{3i}s_i + \mu_i + e_{a,i} \\ \dot{\mu}_i = -k_{4i}\text{sign}(s_i) - k_{5i}s_i \end{cases} \tag{25}$$

where $e_{a,i}$ is the estimation error of the RBF neural network estimator, assuming that it satisfies $|e_{a,i}| \leq \zeta_i|s_i|^{1/2}$ and $e_a = [e_{a,1} \ e_{a,2} \ e_{a,3}]^T$.

Step 1. The Lyapunov function is chosen as follows:

$$V_{s_i} = 2k_{4i}|s_i| + k_{5i}s_i^2 + \frac{1}{2}\mu_i^2 + \frac{1}{2}\left(k_{2i}|s_i|^{1/2}\text{sign}(s_i) + k_{2i}s_i - \mu_i\right)^2 + \frac{1}{2\gamma}e_{a,i}^2 \tag{26}$$

Equation (26) can be written as $V_{s_i} = \eta_i^T \Psi_i \eta_i + \frac{1}{2\gamma}e_{a,i}^2$, where

$$\eta_i = \left[|s_i|^{1/2}\text{sign}(s_i) \ s_i \ \mu_i \right]^T, \ \Psi_i = \frac{1}{2} \begin{bmatrix} 4k_{4i} + k_{2i}^2 & k_{2i}k_{3i} & -k_{2i} \\ k_{2i}k_{3i} & 2k_{5i} + k_{3i}^2 & -k_{3i} \\ -k_{2i} & -k_{3i} & 2 \end{bmatrix}$$

V_{s_i} satisfies the following:

$$\lambda_{\min}\{\Psi_i\} \|\eta_i\|_2^2 \leq V_{s_i} \leq \lambda_{\max}\{\Psi_i\} \|\eta_i\|_2^2 + \frac{\zeta_i^2}{2\gamma}|s_i| \tag{27}$$

Since $|s_i|^{1/2} \leq \|\eta_i\|_2$, it follows that

$$\lambda_{\min}\{\Psi_i\} \|\eta_i\|_2^2 \leq V_{s_i} \leq \left(\lambda_{\max}\{\Psi_i\} + \frac{\zeta_i^2}{2\gamma} \right) \|\eta_i\|_2^2 \tag{28}$$

Deriving the derivative for V_{s_i} , we can obtain the following:

$$\begin{aligned} \dot{V}_{s_i} &= -\frac{1}{|s_i|^{1/2}}\eta_i^T \Theta_i \eta_i - \eta_i^T \Lambda_i \eta_i + e_{a,i} \left(\kappa_{1,i} \eta_i + \frac{1}{|s_i|^{1/2}} \kappa_{2,i} \eta_i \right) + \frac{1}{\gamma} e_{a,i} \dot{e}_{a,i} \\ &= -\frac{1}{|s_i|^{1/2}}\eta_i^T \Theta_i \eta_i - \eta_i^T \Lambda_i \eta_i + e_{a,i} \left(\kappa_{1,i} \eta_i + \frac{1}{|s_i|^{1/2}} \kappa_{2,i} \eta_i - \frac{1}{\gamma} \dot{\hat{w}}_i^T \chi_i \right) \end{aligned} \tag{29}$$

where

$$\Theta_i = \frac{k_{2i}}{2} \begin{bmatrix} 2k_{4i} + k_{2i}^2 & 0 & -k_{2i} \\ 0 & 2k_{5i} + 5k_{3i}^2 & -3k_{3i} \\ -k_{2i} & -3k_{3i} & 1 \end{bmatrix}$$

$$\Lambda_i = k_{3i} \begin{bmatrix} k_{4i} + 2k_{2i}^2 & 0 & 0 \\ 0 & k_{5i} + k_{3i}^2 & -k_{3i} \\ 0 & -k_{3i} & 1 \end{bmatrix}$$

$$\kappa_{1,i} = \left[\frac{3}{2}k_{2i}k_{3i} \ 2k_{5i} + k_{3i}^2 \ -k_{3i} \right], \ \kappa_{2,i} = \left[2k_{4i} + \frac{k_{2i}^2}{2} \ 0 \ -\frac{k_{2i}}{2} \right]$$

Let $\kappa_{1,i} \eta_i + \frac{1}{|s_i|^{1/2}} \kappa_{2,i} \eta_i - \frac{1}{\gamma} \dot{\hat{w}}_i^T \chi_i = 0$; then, the adaptive law can be designed as follows:

$$\dot{\hat{w}}_i = \gamma \left[\left(\kappa_{1i} + \frac{\kappa_{2i}}{|s_i|^{1/2}} \right) \eta_i (\chi_i)^* \right]^T \tag{30}$$

where γ represents the adjustable coefficient associated with the adaptive law, $\gamma > 0$; $(\cdot)^*$ represents the pseudo-converse operation. Thus,

$$\dot{V}_{s_i} = -\frac{1}{|s_i|^{1/2}} \eta_i^T \Theta_i \eta_i - \eta_i^T \Lambda_i \eta_i \tag{31}$$

If Θ_i and Λ_i are positive definite symmetric matrices, then \dot{V}_{s_i} is a negative definite. It is necessary to satisfy $4k_{4i}k_{5i} > (8k_{4i} + 9k_{2i}^2)k_{3i}^2$.

$$\dot{V}_{s_i} \leq -\frac{1}{|s_i|^{1/2}} \lambda_{\min}\{\Theta_i\} \|\eta_i\|_2^2 - \lambda_{\min}\{\Lambda_i\} \|\eta_i\|_2^2 \tag{32}$$

Using Equation (28), it can be derived that

$$\dot{V}_{s_i} \leq -\gamma_{1i} V_{s_i}^{1/2} - \gamma_{2i} V_{s_i} \tag{33}$$

where

$$\gamma_{1i} = \frac{\lambda_{\min}^{1/2}\{\Psi_i\} \lambda_{\min}\{\Theta_i\}}{\lambda_{\max}\{\Psi_i\} + \frac{\zeta_i^2}{2\gamma}}, \quad \gamma_{2i} = \frac{\lambda_{\min}\{\Lambda_i\}}{\lambda_{\max}\{\Psi_i\} + \frac{\zeta_i^2}{2\gamma}}$$

From Lemma 1, if the values of the parameters such as $k_{0i}, k_{1i}, k_{2i}, k_{3i}, k_{4i}$, and k_{5i} are appropriate, the control system can converge to the sliding surface in finite-time.

Step 2. The system reaches the sliding surface, $s_i = 0$, satisfying $|s_i| \leq \varepsilon_i$; then,

$$\dot{e}_i + k_{0i}e_i + k_{1i} \int e_i d\tau = 0 \tag{34}$$

When \dot{s}_i tends to zero, there exists the following:

$$\ddot{e}_i + k_{0i}\dot{e}_i + k_{1i}e_i = 0 \tag{35}$$

The Lyapunov function is chosen as follows:

$$V_e = \frac{1}{2} e^T \dot{e} + \frac{1}{2} \sum_{i=1}^3 k_{1i} e_i^2 = \frac{1}{2} \sum_{i=1}^3 \dot{e}_i^2 + \frac{1}{2} \sum_{i=1}^3 k_{1i} e_i^2 \tag{36}$$

The derivation of Equation (36) yields the following:

$$\dot{V}_e = \sum_{i=1}^3 \dot{e}_i (\ddot{e}_i + k_{1i}e_i) = \sum_{i=1}^3 \dot{e}_i (\ddot{e}_i + k_{1i}e_i) = \sum_{i=1}^3 \dot{e}_i (-k_{0i}\dot{e}_i) = -\sum_{i=1}^3 k_{0i} \dot{e}_i^2 \leq 0 \tag{37}$$

$\dot{V}_e \equiv 0$ is equivalent to $\dot{e}_i \equiv 0$. According to LaSalle’s invariance principle, it can be known that $(e_i = 0, \dot{e}_i = 0)$ is the global asymptotically stable equilibrium point of Equation (34), i.e., $\lim_{t \rightarrow \infty} e_i(t) = \lim_{t \rightarrow \infty} \dot{e}_i(t) = 0$ ($i = 1, 2, 3$). The orbital tracking error e of the system converges asymptotically to zero.

This completes Proof of Theorem 1. \square

3.4. Control Variable Conversion

To achieve station-keeping control, the virtual control acceleration needs to be converted into solar sail cone angle α_s , turning angle δ_s , and solar electric propulsion accelera-

tion a_{ep} after the following is obtained: $\|a_{ep}\| = (a_{ep,x}^2 + a_{ep,y}^2 + a_{ep,z}^2)^{1/2}$. From Equation (12), the solar electric propulsion acceleration components can be derived as follows:

$$\begin{cases} a_{ep,x} = u_1 \cos \theta_s - u_2 \rho_s \sin \theta_s + \beta_s \frac{\sin \alpha_s \cos^2 \alpha_s \sin \delta_s}{\rho_s \|\mathbf{r}_s\|^2} \sin \theta_s - \\ \beta_s \left(\frac{\cos^3 \alpha_s}{\|\mathbf{r}_s\|^3} \rho_s + \frac{\sin \alpha_s \cos^2 \alpha_s \cos \delta_s}{\|\mathbf{r}_s\|^3} z_s \right) \cos \theta_s \\ a_{ep,y} = u_1 \sin \theta_s + u_2 \rho_s \cos \theta_s - \beta_s \frac{\sin \alpha_s \cos^2 \alpha_s \sin \delta_s}{\rho_s \|\mathbf{r}_s\|^2} \cos \theta_s - \\ \beta_s \left(\frac{\cos^3 \alpha_s}{\|\mathbf{r}_s\|^3} \rho_s + \frac{\sin \alpha_s \cos^2 \alpha_s \cos \delta_s}{\|\mathbf{r}_s\|^3} z_s \right) \sin \theta_s \\ a_{ep,z} = u_3 - \beta_s \frac{\cos^3 \alpha_s}{\|\mathbf{r}_s\|^3} z_s - \beta_s \frac{\sin \alpha_s \cos^2 \alpha_s \cos \delta_s}{\|\mathbf{r}_s\|^3} \rho_s \end{cases} \quad (38)$$

where ρ_s, θ_s, z_s , and \mathbf{r}_s are real-time measurement values; the light pressure factor β_s can be found via Equation (39).

$$\beta_s = \left[1 + \left(\frac{z_{s,d}}{\rho_{s,d}} \right)^2 \right]^{1/2} \frac{\left\{ \left(\frac{z_{s,d}}{\rho_{s,d}} \right)^2 + \left[1 - \omega_{s,d}^2 (\rho_{s,d}^2 + z_{s,d}^2)^{3/2} \right]^2 \right\}^{3/2}}{\left\{ \left(\frac{z_{s,d}}{\rho_{s,d}} \right)^2 + \left[1 - \omega_{s,d}^2 (\rho_{s,d}^2 + z_{s,d}^2)^{3/2} \right]^2 \right\}^2} \quad (39)$$

where $\rho_{s,d}, z_{s,d}$, and $\omega_{s,d}$ are nominal parameters of the displaced orbit.

To more directly describe the cost of station-keeping control, real-time mass changes are applied here. The real-time mass change in the electric propellant satisfies the following:

$$\dot{m} = - \frac{\|T\|}{I_{sp} g_0} \quad (40)$$

where T is the electric thrust, $T = [T_x \ T_y \ T_z]^T$, and $\|T\| = m \|a_{ep}\|$; I_{sp} is the specific impulse of electric propulsion; and g_0 is the standard gravitational acceleration of Earth.

The propellant consumption can be reduced by solving the minimum value of electric propulsion acceleration using the following expression:

$$(\alpha, \delta) = \underset{\substack{\alpha_s \in [-\pi/2, \pi/2] \\ \delta_s \in [-\pi, \pi]}}{\operatorname{argmin}} (\|a_{ep}\|) \quad (41)$$

where α and δ , respectively, are the cone angle and turning angle, which are optimal solutions for propellant consumption. On the basis of the optimal solutions, the electric thrust T can be obtained.

4. Simulation Results and Discussion

4.1. Simulation Conditions

The studied nominal heliocentric displaced orbit is located above the ecliptic plane. The nominal orbit always has the same phase as Earth, with a period of 1 year. The dimensionless parameters of the heliocentric displaced orbit are shown in Table 1. From Equation (39), the light pressure factor can be calculated as 0.7356, which is less than 1 and can be realized for engineering applications.

Table 1. Parameters of nominal heliocentric displaced orbit.

Orbital Radius	Displaced Height	Angular Velocity
0.7AU	0.4AU	1

It is assumed that the initial mass of the solar sail spacecraft is 500 kg. The combination of a slider and RSB was used as the propellant-free actuator, and the argon Hall thruster was used as the solar electric thruster. The relevant parameters of the argon Hall thruster are shown in Table 2.

Table 2. Parameters of argon Hall thruster.

Propellant	Thrust (mN)	Specific Impulse (s)	Total Efficiency	Power (kW)	Mass (kg)
Argon	170	2500	50%	4.2	2.1

The relevant parameters of the adaptive sliding mode controller for station-keeping are shown in Table 3.

Table 3. Parameters of adaptive sliding mode controller.

Parameters of the Sliding Surface	Parameters of the Approaching Law	Parameters of the Adaptive Law
$k_{0i} = 165; k_{1i} = 0.0003;$ $\varepsilon_i = 0.00001; \tau_i = -0.98$	$k_{2i} = 1; k_{4i} = 0.001$	$\gamma = 0.001$

We assumed that the orbital radius error and the displaced height error of the solar sail spacecraft in the heliocentric displaced orbit at the initial injection were 10,000 km and $-10,000$ km, respectively. The simulation step was set to 0.000001 TU (1 TU \approx 58 d) and the simulation time was set to 365 d.

Referring to the simulation conditions in the literature [29,30], the dimensionless external disturbance acceleration a_d and the internal unmodeled dynamics $a_{\Delta f}$ were set as follows:

$$\begin{cases} a_{d_1} = 0.00001 \sin(80t + 100) \\ a_{d_2} = 0.00001 \cos(60t - 100) \\ a_{d_3} = 0.00001 (\sin(80t) + 1) \end{cases}, \begin{cases} a_{\Delta f_1} = 0.01[\rho_s - \cos(5\theta_s - 0.1)] / \|\mathbf{r}_e\|^3 \\ a_{\Delta f_2} = -0.01 \sin(2\theta_s) / (\rho_s \|\mathbf{r}_e\|^3) \\ a_{\Delta f_3} = -0.01 z_s \sin(3\theta_s + 0.1) / \|\mathbf{r}_e\|^3 \end{cases}$$

where \mathbf{r}_e denotes the position vector of the geocenter with respect to the solar sail spacecraft.

4.2. Simulation Results and Discussion under Different Sources of Disturbance

Simulations under different sources of perturbations will be studied in the following sections. To further verify the effectiveness of the adaptive sliding mode station-keeping control strategy proposed in this paper, the orbit position tracking error results were compared with the literature [28–30].

4.2.1. When the Solar Sail Spacecraft Is Mainly Subjected to External Disturbances

The simulation results of the station-keeping control are shown in Figures 3–8.

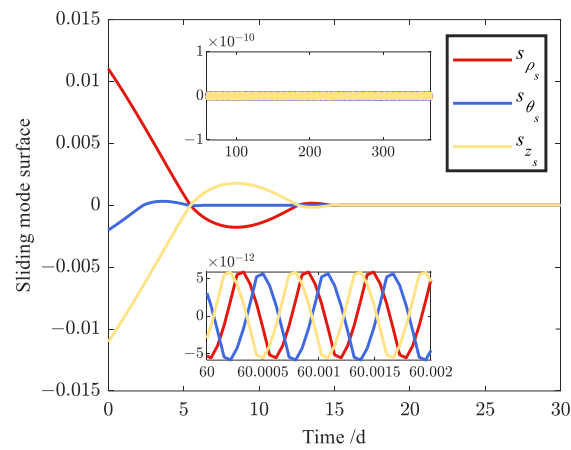


Figure 3. Change curves of improved integral sliding surfaces.

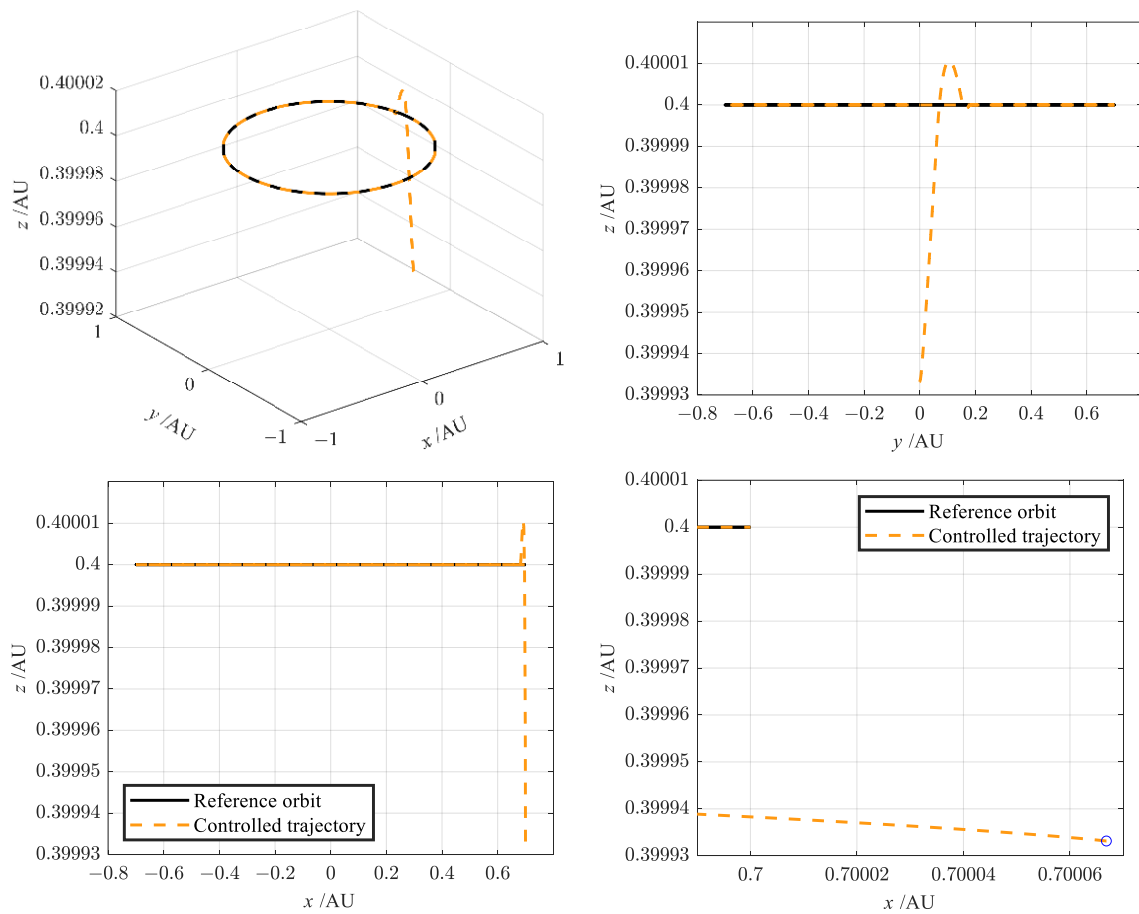


Figure 4. Reference orbit and controlled trajectory.

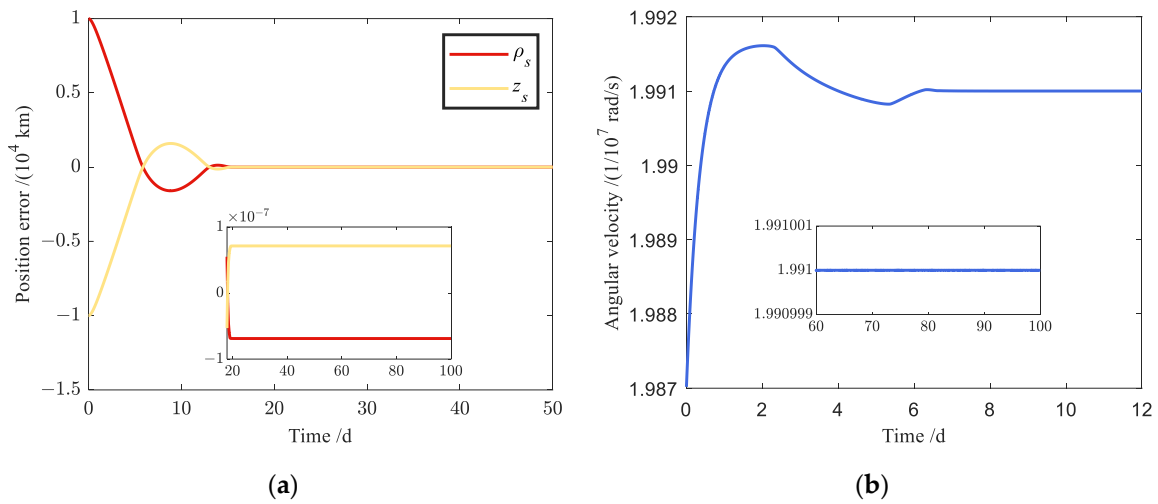


Figure 5. Change curves of position errors and angular velocity: (a) change curves of orbital radius error and displaced height error; (b) change curve of angular velocity.

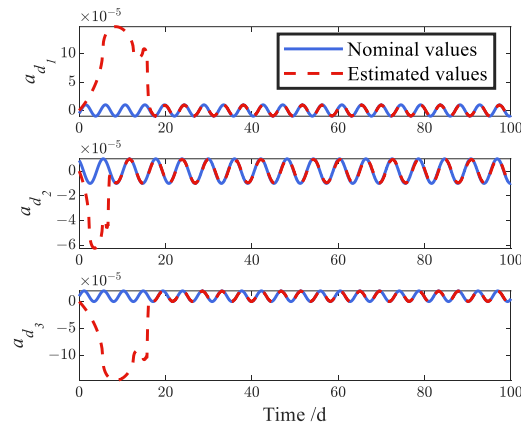


Figure 6. Change curves of external disturbances and their estimations.

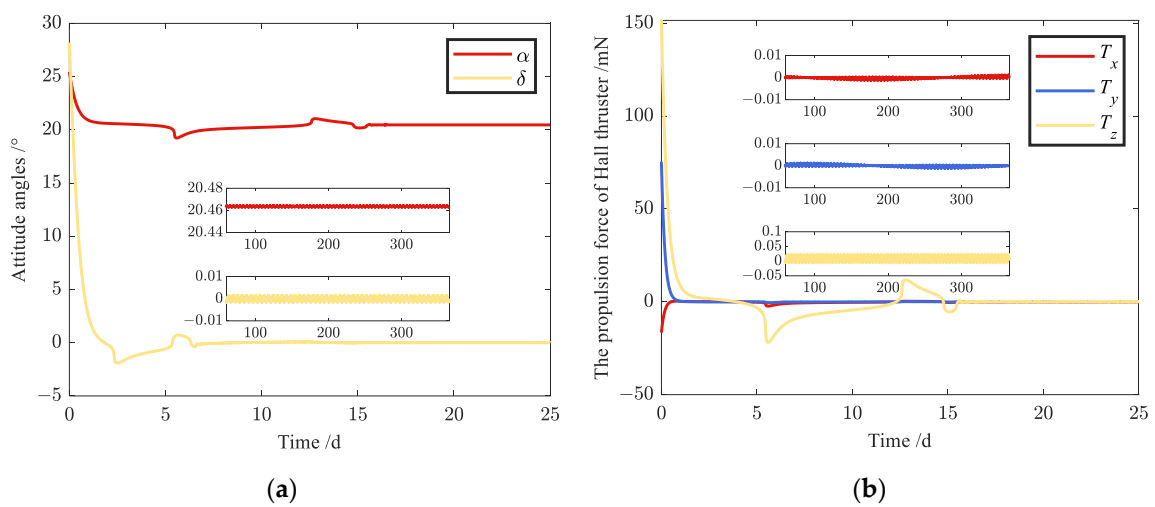


Figure 7. Station-keeping control variables: (a) change curves of attitude angles; (b) change curves of propulsion force components of argon Hall thruster.

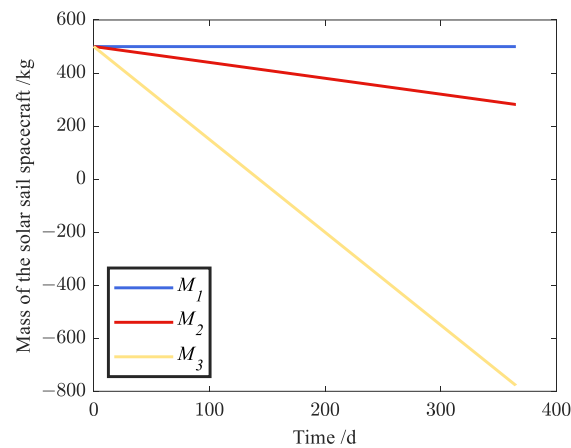


Figure 8. Mass variation in a spacecraft under different propulsion methods.

Figure 3 shows the response curve of the improved integral sliding surface. The sliding surface eventually converges to near zero. Figure 4 describes the trajectory of the solar sail spacecraft under the action of the proposed high-performance station-keeping control strategy. The black solid line represents the reference orbit and the yellow dashed line represents the actual trajectory. It can be seen from Figure 4 that the two overlap well, indicating that the station-keeping control strategy proposed in this paper has good accuracy. Figure 5 shows the response curves of orbital position errors and angular velocity. The orbital radius error and displaced height error converge to within 0.8 m after 20 d, and the orbital angular velocity converges to the nominal angular velocity after 8 days.

Figure 6 shows the estimation results of the RBF neural network estimator for the external disturbance acceleration. It can be seen that, during the spacecraft's approach to the nominal orbit, the estimator's performance in estimating disturbance acceleration is not ideal. However, when the orbital angular velocity converges to the nominal angular velocity, the estimation of a_{d_2} is enhanced. When the orbital position tends to be stable, the estimator's estimate of each component of the disturbance acceleration can better approximate the actual value.

Figure 7 shows the results of the control variables in the case of minimum propellant consumption. From Figure 7, it can be seen that the cone angle and turning angle stabilize to 20.464° and -0.001° , respectively, after 15 days, and the propulsion force of the argon Hall electric thruster stabilizes within 0.02 mN after 15 days.

Figure 8 describes the mass variation in the solar sail spacecraft under different propulsion methods. M1 represents the mass variation when a hybrid propulsion method is used; M2 represents the mass variation when the argon Hall electric thruster is operating at maximum power; and M3 represents the mass variation when only electric thrusters are used for propulsion. Throughout one year, M1 decreases by 0.46 kg and M2 decreases by 218.67 kg, while the amount of change in M2 is much smaller than M3, which means that a single electric thruster cannot accomplish the station-keeping control mission. Therefore, hybrid propulsion is currently the most efficient way to achieve the station-keeping control of a solar sail spacecraft.

4.2.2. When the Solar Sail Spacecraft Is Subjected to Both External Disturbances and Internal Unmodeled Dynamic

Figure 9 shows the response curves of orbital position errors and angular velocity. Similar to the results in Section 4.2.1, the orbital radius error and displaced height error converge to within 0.8 m after 20 d, and the orbital angular velocity converges to the nominal angular velocity after 8 days.

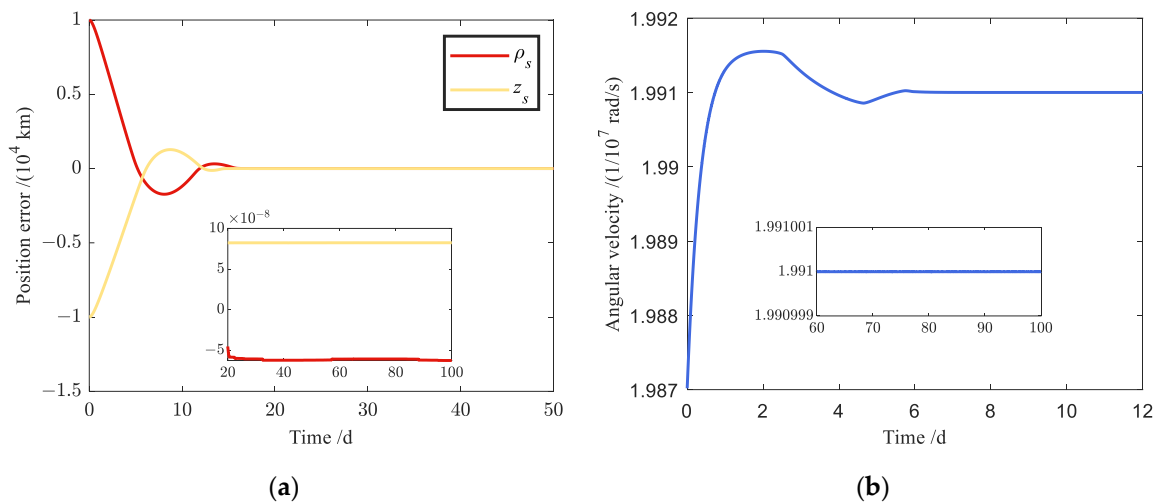


Figure 9. Change curves of position errors and angular velocity: (a) change curves of orbital radius error and displaced height error; (b) change curve of angular velocity.

Figure 10 shows the estimation results of the RBF neural network estimator for the combined disturbance acceleration. Similar to the results in Section 4.2.1, the estimation in the transition stage is unsatisfactory, while in the steady state, the estimated value is able to approximate the actual value well.

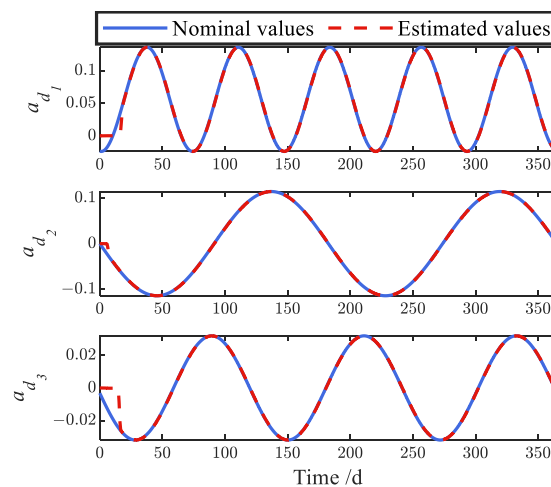


Figure 10. Change curves of external disturbances and their estimations.

Figure 11 shows the results of the control variables in the case of minimum propellant consumption. As can be seen from Figure 11, the cone and turning angles oscillate and change during the one-year running period, and, in particular, the turning angle has a large range of variation, which means that the orientation of the sail surface is always changing. From a comparison with Section 4.2.1, it was found that the unmodeled dynamics are the main reason for the obvious change in attitude angles in Figure 11. This is due to the relatively large order of magnitude of the unmodeled dynamics. The thrust of the argon Hall thruster changes correspondingly with the change in attitude angles.

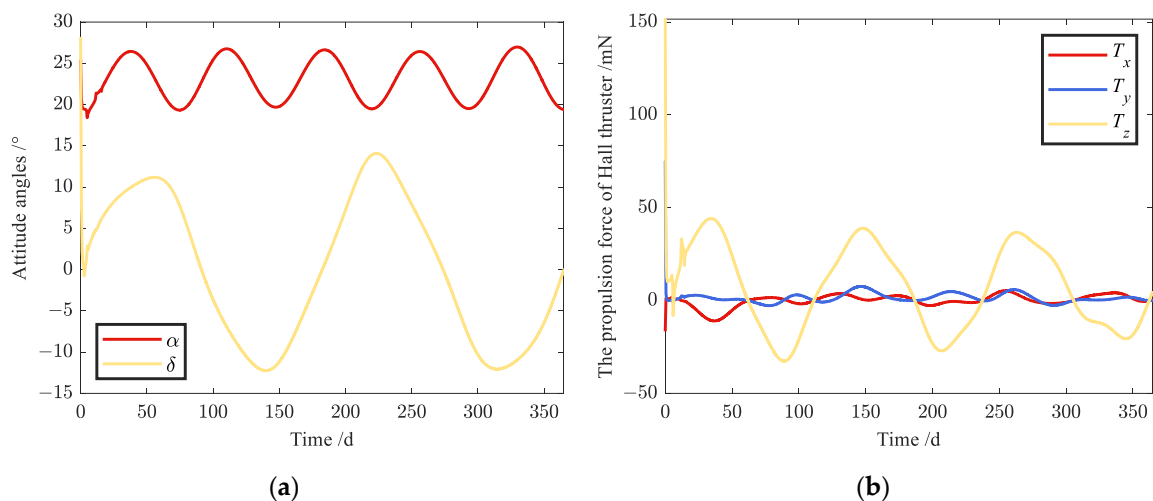


Figure 11. Station-keeping control variables: (a) change curves of attitude angles; (b) change curves of propulsion force components of argon Hall thruster.

Figure 12 describes the mass variation in a solar sail spacecraft. After one year, M_1 decreases by 26.69 kg. Considering argon prices, mass requirements for solar sail spacecraft, and launch costs, it can be found that hybrid propulsion has more obvious advantages for long-period missions such as heliocentric displaced orbits. In addition to this method of minimizing propellant consumption, a single electric thruster can be used to achieve station-keeping control under a given attitude angle. Of course, this method requires higher mass of the propellant to be consumed.

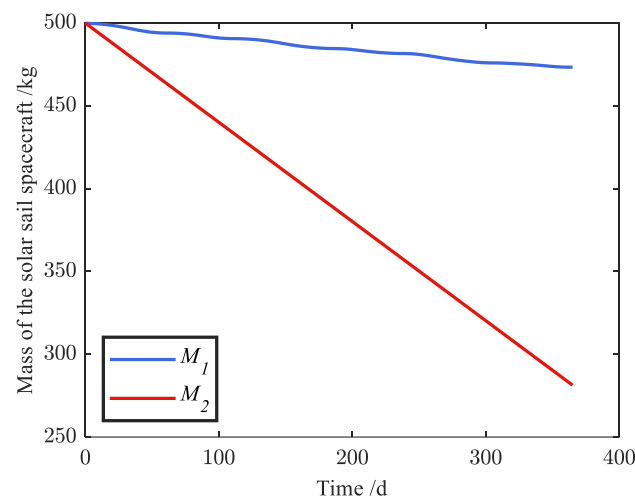


Figure 12. Mass variation in a spacecraft.

4.2.3. Comparison of Simulation Results

Since the simulation conditions are consistent, the results of the comparison between the proposed station-keeping control strategy and the other three control strategies in terms of orbit position errors will be given directly here, as shown in Table 4. As can be seen from Table 4, the adaptive sliding mode controller proposed in this paper has faster station tracking speed and higher control accuracy compared with existing controllers.

Table 4. Comparison of orbit tracking position errors.

	Maximum Thrust of Electric Thruster (mN)	Convergence Time (d)	Orbital Radius Tracking Error (km)	Displaced Height Tracking Error (km)
In this article	170	20	−0.0006	0.0008
In the literature [28]	230	40	−0.0012	0.0016
In the literature [29]	230	90	Within 0.05	Within 0.05
In the literature [30]	230	730	−30.0006	−198.9652

From the above simulation results, it is clear that the proposed station-keeping control strategy has the following characteristics: (1) the tracking position errors can reach the order of decimeters, close to zero; (2) the steady-state errors of orbit tracking under different sources of disturbances are in the same order of magnitude, and are nearly the same size; and (3) the values of the relevant parameters of the station-keeping controller under different sources of disturbances are consistent.

5. Conclusions

In this paper, an adaptive high-performance sliding mode control strategy was designed to solve the station-keeping control problem of the heliocentric displaced orbit. An RBF neural network estimator was designed, which achieved online estimation and compensation of the combined disturbance acceleration of each channel; an adaptive orbit-keeping controller based on the improved integral sliding surface and multivariate super-twisting sliding mode convergence law was designed, which achieved fast tracking of the nominal orbit with high control accuracy. The simulation results showed that the proposed station-keeping control strategy has strong robustness and a fast orbit tracking speed, with position tracking errors up to decimeters.

Author Contributions: Conceptualization, T.Z. and R.M.; methodology, T.Z.; software, T.Z.; validation, T.Z., Y.Z. and Z.L.; formal analysis, T.Z.; investigation, T.Z. and Y.Z.; resources, T.Z., Z.Z., B.L. and C.Y.; data curation, T.Z. and Z.L.; writing—original draft preparation, T.Z.; writing—review and editing, R.M., Y.Z., Z.L., Z.Z., B.L. and C.Y.; visualization, T.Z.; supervision, R.M., Z.Z., B.L. and C.Y.; project administration, R.M.; funding acquisition, R.M., Z.Z., B.L. and C.Y. All authors have read and agreed to the published version of the manuscript.

Funding: This research was funded by the Shanghai Institute of Satellite Engineering (SISE) and by the pre-research on civilian space technology, grant number D010301. The APC was funded by the Institute of Aircraft Systems Engineering.

Data Availability Statement: The data presented in this study are available upon request from the corresponding author.

Acknowledgments: We would like to thank SISE for funding; the relevant engineering data that SISE provided assisted us significantly.

Conflicts of Interest: The authors declare no conflict of interest.

References

1. Yang, J. Thinking on the Development of China's Cause. *Important Issues* **2017**, *11*, 1–2. [[CrossRef](#)]
2. Yin, J.; Zhang, R.; Zhang, X. Orbital Dynamic Characters and Orbital Maintenances of Pole-sitter Spacecraft. *Spacecr. Eng.* **2018**, *27*, 26–34.
3. Ullery, D.C.; Soleymani, S.; Heaton, A.; Orphee, J.; Johnson, L.; Sood, R.; Kung, P.; Kim, S.M. Strong Solar Radiation Forces from Anomalous Reflecting Metasurfaces for Solar Sail Attitude Control. *Sci. Rep.* **2018**, *8*, 10026. [[CrossRef](#)] [[PubMed](#)]
4. Baoyin, H.; McInnes, C.R. Solar sail orbits at artificial Sun-Earth libration points. *J. Guid. Control Dyn.* **2005**, *28*, 1328–1331. [[CrossRef](#)]
5. Zhang, J.; Cao, X.; Liu, W.; She, W.; Wei, J. Orbit keeping and control of solar sail spacecraft with RCD on artificial libration points. *Flight Dyn.* **2021**, *39*, 77–81.

6. Bianchi, C.; Niccolai, L.; Mengali, G.; Quarta, A.A. Collinear artificial equilibrium point maintenance with a wrinkled solar sail. *Aerosp. Sci. Technol.* **2021**, *119*, 107150. [[CrossRef](#)]
7. Simo, J.; McInnes, C.R. Displaced solar sail orbits: Dynamics and applications. *Adv. Astronaut. Sci.* **2010**, *136*, 1803–1816.
8. Ceriotti, M.; McInnes, C.R. Hybrid solar sail and solar electric propulsion for novel Earth observation missions. *Acta Astronaut.* **2011**, *69*, 809–821. [[CrossRef](#)]
9. Li, Z.; Yuan, C.; Yu, H.; Zuo, C. Station-Keeping Control of Solar Sail Spacecraft Planet-Centred Displaced Orbit. *J. Spacecr. Rockets* **2019**, *45*, 33–37.
10. Niccolai, L.; Mengali, G.; Quarta, A.A.; Caruso, A. Feedback control law of solar sail with variable surface reflectivity at Sun–Earth collinear equilibrium points. *Aerosp. Sci. Technol.* **2020**, *106*, 106144. [[CrossRef](#)]
11. Moore, L.; Ceriotti, M.; McInnes, C.R. Station-keeping for a solar sail during lander/probe deployment using feedback control. *Acta Astronaut.* **2022**, *201*, 182–197. [[CrossRef](#)]
12. Moore, L.; Ceriotti, M. Solar sails for perturbation relief: Application to asteroids. *Adv. Space Res.* **2021**, *67*, 3027–3044. [[CrossRef](#)]
13. Gong, S.; Li, J.; Simo, J. Orbital motions of a solar sail around the L2 Earth–Moon libration point. *J. Guid. Control Dyn.* **2014**, *37*, 1349–1356. [[CrossRef](#)]
14. Yuan, J.; Gao, C.; Zhang, J. Periodic orbits of solar sail equipped with reflectance control device in Earth–Moon system. *Astrophys. Space Sci.* **2018**, *363*, 23. [[CrossRef](#)]
15. Zhu, M. Dynamics and Control of Solar Sail Spacecraft. Ph.D. Thesis, University of Science and Technology of China, Hefei, China, 2016.
16. Lou, Z.; Zhang, K.; Wang, Y.; Gao, Q. Active disturbance rejection station-keeping control for solar-sail libration-point orbits. *J. Guid. Control Dyn.* **2016**, *39*, 1913–1917. [[CrossRef](#)]
17. Lou, Z. Dynamics and Control of Continuous Low-Thrust Spacecraft on Libration Points. Ph.D. Thesis, University of Science and Technology of China, Hefei, China, 2019.
18. Huang, J.; Biggs, J.D.; Bai, Y.; Cui, N. Integrated guidance and control for solar sail station-keeping with optical degradation. *Adv. Space Res.* **2021**, *67*, 2823–2833. [[CrossRef](#)]
19. Huang, J.; Bai, Y.; Biggs, J.D.; Cui, N. Indirect Estimation Based Active Disturbance Rejection Control for Solar Sail Station-Keeping. *Int. J. Aeronaut. Space Sci.* **2021**, *22*, 1493–1503. [[CrossRef](#)]
20. Heiligers, J.; McInnes, C.R.; Biggs, J.D.; Ceriotti, M. Displaced geostationary orbits using hybrid low-thrust propulsion. *Acta Astronaut.* **2012**, *71*, 51–67. [[CrossRef](#)]
21. Simo, J.; McInnes, C.R. Designing displaced lunar orbits using low-thrust propulsion. *J. Guid. Control Dyn.* **2010**, *33*, 259–265. [[CrossRef](#)]
22. Simo, J.; McInnes, C.R. Feedback stabilization of displaced periodic orbits: Application to binary asteroids. *Acta Astronaut.* **2014**, *96*, 106–115. [[CrossRef](#)]
23. Heiligers, J.; Ceriotti, M.; McInnes, C.R.; Biggs, J.D. Displaced geostationary orbit design using hybrid sail propulsion. *J. Guid. Control Dyn.* **2012**, *34*, 1852–1866. [[CrossRef](#)]
24. SpaceX just Announced Their Hall Thruster Parameters, actually Ar Propellant. Available online: <https://m.163.com/dy/article/HUMMT1QL05119RIN.html> (accessed on 22 April 2023).
25. McKay, R.; Macdonald, M.; Biggs, J.; McInnes, C. Survey of highly non-Keplerian orbits with low-thrust propulsion. *J. Guid. Control Dyn.* **2011**, *34*, 645–666. [[CrossRef](#)]
26. McInnes, C.R. Passive control of displaced solar sail orbits. *J. Guid. Control Dyn.* **1998**, *21*, 975–982. [[CrossRef](#)]
27. Bookless, J.; McInnes, C. Dynamics and control of displaced periodic orbits using solar-sail propulsion. *J. Guid. Control Dyn.* **2006**, *29*, 527–537. [[CrossRef](#)]
28. Qian, H.; Zheng, J.; Yu, X.; Gao, L. Dynamics and control of displaced orbits for solar sail spacecraft. *Chin. J. Space Sci.* **2013**, *33*, 458–464. [[CrossRef](#)]
29. Zhang, K.; Lou, Z.; Wang, Y.; Chen, S. Station-keeping control of spacecraft using hybrid low-thrust propulsion in heliocentric displaced orbits. *Acta Aeronaut. Astronaut. Sin.* **2015**, *36*, 3910–3918.
30. Chen, Y.; Qi, R.; Zhang, J.; Wang, H. High-performance sliding mode control for orbit keeping of spacecraft using hybrid low-thrust propulsion. *Acta Aeronaut. Astronaut. Sin.* **2019**, *40*, 322827.
31. Yu, S.; Yu, X.; Shirinzadeh, B.; Man, Z. Continuous finite-time control for robotic manipulators with terminal sliding mode. *Automatica* **2005**, *41*, 1957–1964. [[CrossRef](#)]

Disclaimer/Publisher’s Note: The statements, opinions and data contained in all publications are solely those of the individual author(s) and contributor(s) and not of MDPI and/or the editor(s). MDPI and/or the editor(s) disclaim responsibility for any injury to people or property resulting from any ideas, methods, instructions or products referred to in the content.